Local electronic structure of dilute hydrogen in β-MnO$_2$

H. Okabe,[1] M. Hiraishi,[1] A. Koda,[1,2] S. Takeshita,[1,2] K. M. Kojima,[3] I. Yamauchi [4] T. Ohsawa [5] N. Ohashi [5]
H. Sato,[6] and R. Kadono [1,2,*]

[1]*Muon Science Laboratory and Condensed Matter Research Center, Institute of Materials Structure Science,*
High Energy Accelerator Research Organization (KEK-IMSS), Tsukuba, Ibaraki 305-0801, Japan
[2]*Department of Materials Structure Science, The Graduate University for Advanced Studies (Sokendai), Tsukuba, Ibaraki 305-0801, Japan*
[3]*Centre for Molecular and Materials Science TRIUMF, Vancouver, B.C., Canada V6T 2A3*
[4]*Graduate School of Science and Engineering, Saga University, Saga 840-8502, Japan*
[5]*National Institute for Materials Science (NIMS), Tsukuba, Ibaraki 305-0044, Japan*
[6]*Department of Physics, Chuo University, Tokyo 112-8551, Japan*

The electronic and magnetic states of β-MnO$_2$ in terms of hydrogen impurities have been investigated by the muon spin rotation technique combined with density-functional theory (DFT) calculations for muon as pseudohydrogen. We found that 85% of implanted muons are localized in the oxygen channels of the rutile structure and behave like interstitial protons (Mu$^+$) except those (7.6%) forming a charge-neutral state (Mu^0) at 2.3 K, which indicates that interstitial hydrogen acts like a shallow donor within less than 0.1 meV of ionization energy. The residual 15% of muons are attributed to those related to lattice imperfection as Mn vacancies. Detailed analyses combined with the DFT approach suggested that the muon is localized at the center of the oxygen channel due to its large zero-point vibration energy.

I. INTRODUCTION

Manganese dioxide (MnO$_2$) is well known as a catalyst for a variety of chemical reactions, such as the deoxidization process of hydrogen peroxide, which we know from elementary school chemistry. Most recently, it has been attracting a great deal of attention as a highly efficient heterogeneous catalyst for the oxidation of various types of substrates, including biomass-derived compounds [1]. Most applications of MnO$_2$ are in batteries; MnO$_2$ synthesized by the electrolytic method (γ-MnO$_2$) is used worldwide as the cathode material in lithium or zinc primary batteries [2]. Artificially synthesized MnO$_2$ generally contains hydrogen in the crystal structure, which is believed to influence various physical, chemical, and electrochemical properties.

There are two types of hydrogens (protons) existing in γ-MnO$_2$, as proposed by Ruetschi and Giovanoli [3–5]. The first type are protons associated with cation vacancies, termed "Ruetschi" protons, which compensate for the charge instead of Mn^{4+} cations. The second type are protons associated with Mn^{3+} cations, termed "Coleman" protons, which are located in the tunnels of the structure, and they are more mobile than Ruetschi protons. The existence of these two types of protons has been confirmed experimentally by neutron diffraction and NMR studies [6–10]. However, these protons are mainly distinguished by differences in O–H bond lengths, therefore their specific positions and electronic states remain unclear.

The main reason for this problem is the difficulty of detecting dilute amounts of hydrogen.

Since hydrogen is the lightest and smallest of all the elements, and because of its ubiquitous presence in nature, it easily penetrates into materials to cause embrittlement of metals, and it serves as a possible source for unintentional carrier doping in semiconductors [11,12]. Nevertheless, it is difficult to ascertain the behavior of dilute hydrogen in matter due to its own weak signals and/or the false detection of background-originated signals from extraneous hydrogen in various diffraction analyses. It is therefore desirable to develop an effective method to ascertain the behavior of hydrogen in host materials.

To obtain microscopic information on the local electronic structure of isolated hydrogen in matter, positive muon studies have been making significant contributions. While a positive muon as pseudohydrogen exhibits a remarkable isotope effect for the kinetics of muon/proton in matter, its local electronic structure as an atom determined by muon-electron interaction (resulting in various charged states designated as Mu$^+$, Mu^0, or Mu$^-$) is almost identical to that of hydrogen. Thus, implanted muon can be regarded as a simulator for the electronic structure of interstitial hydrogen. We previously identified the electronic structure of muons in oxide semiconductors using the muon spin rotation (μSR) technique, and we found evidence for hydrogen impurities as a possible origin of unintentional n-type conductivity [13–21].

As part of our continued effort to elucidate the behavior of hydrogen in oxide semiconductors, we focused on β-MnO$_2$ as our next research target. MnO$_2$ is known to exhibit a variety of crystalline polymorphs, which results in various tunnel and

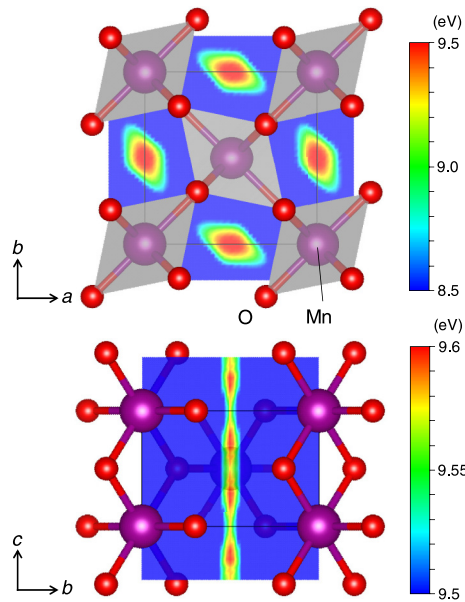*Author to whom all correspondence should be addressed: ryosuke.kadono@kek.jp

FIG. 1. Crystal structure and electrostatic potential maps for β-MnO$_2$ calculated by using reported lattice parameters [25]. The Hartree potential calculated using VASP is represented by the color contour from blue to red in the lattice planes (002) and (100). The solid lines indicate the unit cell.

layered structures [22], where β-MnO$_2$ (pyrolusite) is the simplest and most thermodynamically stable phase. The crystal structure of β-MnO$_2$ consists of MnO$_6$ octahedra shared by corners or edges with 1×1 tunnels (oxygen channels; see Fig. 1), which is also part of the basic structure of γ-MnO$_2$. Note that the structure of β-MnO$_2$ is identical to that of rutile (TiO$_2$), which has been studied intensively by μSR [17,18].

β-MnO$_2$ is regarded as a narrow-gap semiconductor, and it is known to exhibit *n*-type conductivity [23,24]. The *n*-type nature of β-MnO$_2$ may stem from oxygen deficiency and/or lesser impurity interstitials such as hydrogen. If the oxygen vacancy concentration is negligibly small, hydrogen could be a major source of carriers. However, it is often difficult to separate all of these different contributions in bulk property measurements. On the other hand, μSR can provide useful information in order to extract intrinsic electronic properties out of those extrinsic contributions because muon monitors local magnetic states in the atomic scale. Even more conveniently, β-MnO$_2$ is known as a classical example of magnetic materials with a well-defined screw magnetic order below $T_N = 92$ K [26,27]. Since a muon is a direct probe of local magnetic fields, we can determine the position and the electronic state of hydrogen in β-MnO$_2$ by μSR using the magnetic structure as a guide.

In this work, we used muon as a microscopic simulator for extrinsic hydrogen/proton to identify the local electronic and magnetic structures stemming from interstitial hydrogen in β-MnO$_2$ by probing the local fields from the surrounding Mn ions that exhibit well-defined magnetic order. The paper proceeds as follows. Section II describes the sample characterization, the μSR experiment, and computational details. Section III presents the results of transverse-field (TF) μSR, zero-field (ZF) μSR measurements, and density functional

theory (DFT) calculations. Then, we discuss the positions of hydrogen and the effect on the electronic and magnetic state of β-MnO$_2$. Finally, Sec. IV summarizes this paper.

II. EXPERIMENTAL DETAILS

A powder sample of β-MnO$_2$ (3N, Soekawa Co., Ltd.) was used in the present study. The crystal structure and phase purity were checked using a Rigaku MultiFlex powder x-ray diffractometer under ambient conditions with Cu $K\alpha$ radiation. The XRD data indicate that the sample crystallized into β-MnO$_2$ single phase and the absence of a secondary phase (see the Supplemental Material [28], Fig. S1).

The hydrogen content in the sample was observed by thermal desorption spectrometry (TDS) placed in the National Institute for Material Science (NIMS). The sample was linearly heated from room temperature to 1073 K in 2 h and kept at 1073 K for 1 h. During the heating, the amount of desorbed hydrogen was measured by a quadrupole mass spectrometer (QMS). The QMS signal intensity of a hydrogen molecule from the sample increased with increasing temperature, and 2.918×10^{19} cm^{-3} of hydrogen was detected (Fig. S2).

The magnetic susceptibility χ was measured using a Quantum Design SQUID magnetometer from 5 to 400 K. The temperature dependence of χ shows a kink at 92 K, corresponding to the Néel temperature of β-MnO$_2$ (Fig. S3). The peak anomaly around 40 K is probably due to hydrogen impurities, since it was suppressed after heat treatment at 723 K in air. χ also shows Curie-Weiss behavior with the Curie constant $C = 2.51$ emu K/mol and the Weiss temperature $\Theta = -788$ K, which are in good agreement with the earlier report [24] (Fig. S3, inset).

Conventional μSR experiments were performed using the ARTEMIS spectrometer installed in the S1 area at Muon Science Establishment (MUSE), Japan Proton Accelerator Research Complex (J-PARC). Time-dependent μ-e decay asymmetry $A(t)$ was measured to monitor the local field under zero field (ZF), longitudinal field (LF), and weak transverse field (TF) conditions. Additional μSR experiments were conducted to resolve the detailed local field distribution using two instruments, i.e., the LAMPF spectrometer on the M20 beamline, and the NuTime spectrometer on the M15 beamline at TRIUMF, Canada, for the magnetic and paramagnetic phases of β-MnO$_2$, respectively. The μSR spectra have been analyzed using the MUSRFIT software package [29].

The DFT calculations were performed using the projector augmented wave approach [30] implemented in the Vienna Ab initio Simulation Package (VASP) [31] with the Perdew-Burke-Ernzerhof (PBE) exchange correlation potential [32]. The cutoff energy for the plane-wave basis set was 500 eV. All atoms were relaxed until the Hellmann-Feynman forces on them were smaller than 0.01 eV/Å. The distribution of the local magnetic field at the muon sites was calculated using the DIPELEC program [33]. Crystal structures were visualized using the VESTA program [34].

III. RESULTS AND DISCUSSION

A. Local fields in the paramagnetic phase

At first, we attempted to narrow down the position of hydrogen/muon in a β-MnO$_2$ structure by examining the
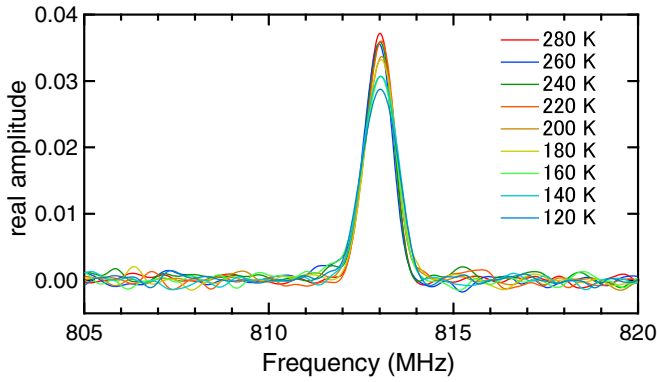
FIG. 2. Fast Fourier transform of the μSR time spectra measured under a transverse field of 6 T.

local field in the paramagnetic phase. The local field provides useful information for identifying the muon stopping site, because it is mainly determined by the spatial arrangement of the nearest-neighboring (nn) Mn d-electrons. As shown in Fig. 1, it is suggested from our preliminary calculation using VASP that the Hartree potential for the interstitial Mu$^+$ exhibits minima around the center of the oxygen channels along the c-axis direction. When an external magnetic field is applied transverse to the initial muon polarization vector, the muon exhibits spin precession at a frequency corresponding to the summation of the external and internal fields. Thus, by evaluating the shift from the reference frequency of the external field, one can extract the contribution of the internal field at a particular stopping site from the TF-μSR spectrum.

Figure 2 shows the fast Fourier transform (FFT) of TF-μSR spectra under a transverse field of 6 T obtained at various temperatures. One can see a single Gaussian-like line shape at around 813 MHz, where the slight broadening of the linewidth with decreasing temperature is probably due to the gradual development of staggered magnetization related to the short-range magnetic order [24,27]. To interpret the line shape of these spectra, we calculated the frequency distribution in a polycrystalline sample (powder pattern) for several candidate muon sites [35].

The calculated powder patterns of putative muon sites are shown in Fig. 3 with additional Gaussian broadening due to the local field inhomogeneity and the truncation of Fourier transforms by the finite time window ($t \leqslant 10 \ \mu$s). These muon sites have been selected by considering the electrostatic potential maps (see Fig. 1) and the distance from nn O ions. The line shape has two edges determined by the anisotropy of the hyperfine coupling ($A_\parallel$ and $A_\perp$), which is related to the local χ induced by the nn Mn spins. One can see that the muon site near a certain Mn ion, e.g., the $2b$ site $(0,0,1/2)$, shows a marked asymmetric feature with a broad distribution. Since the experimental spectra show no signs of these shoulderlike features, implanted muons tend to be located away from Mn ions, at a high-symmetry position in the Mn sublattice. A comparison of the spectra with that simulated for the O defect position (vacancy) also infers that muons have little chance to find O vacancies within their lifetime.

Considering previous neutron and NMR studies [6–10], it is reasonable to assume that muons are localized near the center of the oxygen channel in the rutile structure. Our result further suggests that muons do not occupy low-symmetry positions including oxygen vacancies. On the other hand, there remains a possibility that muons are localized in Mn vacancies due to the lack of frequency resolution (see the line shape at the Mn defect position in Fig. 3). Therefore, additional information is needed to resolve this issue (see the next section).

B. Local fields in the magnetically ordered phase

β-MnO$_2$ undergoes a helical magnetic transition at $T_N = 92$ K with incommensurate magnetic modulation [propagation vector $q_m = (0, 0, \sim 2/7)$] without much temperature dependence [26,27]. Given that the magnetic structure is already known, a spontaneous long-range magnetic order is often helpful to identify the muon sites by comparing the observed field distribution with that calculated for the candidate sites using the known magnetic structure.

Figure 4(a) shows a ZF-μSR time spectrum at 2.5 K for the sample from the same batch used in the TF measurements. One can see a clear oscillation in the early time domain ($<0.25 \ \mu$s), implying long-range magnetic order. The FFT spectrum [Fig. 4(b)] indicates that the oscillating signal is dominated by two frequency components ($f_1 \simeq 97$ and $f_2 \simeq 124$ MHz). While this feature is usually attributed to the presence of two distinct muon sites, it turns out to be not necessarily the case in β-MnO$_2$.

For an incommensurate magnetic structure under zero field, the local field distribution $D(B_{\text{loc}})$ is given by

$$D(B_{\text{loc}}) = \frac{2}{\pi} \frac{B_{\text{loc}}}{\sqrt{B_{\text{loc}}^2 - B_{\text{min}}^2}\sqrt{B_{\text{max}}^2 - B_{\text{loc}}^2}},$$

where it has two characteristic cutoff fields (B_{min} and B_{max}) [36]. Unfortunately, the muon polarization function in the time domain associated with $D(B_{\text{loc}})$ cannot be obtained analytically. We adopt an approximate distribution, which is called the shifted-Overhauser distribution $D'(B_{\text{loc}})$,

$$D'(B_{\text{loc}}) = \frac{1}{\pi} \frac{1}{\sqrt{B_{\text{dif}}^2 - (B_{\text{loc}} - B_{\text{av}})^2}},$$

where $B_{\text{dif}} = (B_{\text{max}} - B_{\text{min}})/2$, and $B_{\text{av}} = (B_{\text{max}} + B_{\text{min}})/2$ is used for the incommensurate case [37]. According to this approximation, the oscillatory part of the muon polarization function is written by the product of the zeroth-order Bessel function and the cosine function.

Based on the above approximation, we analyzed the spectrum using the following curve-fit function:

$$A(t) = A_T J_0(\gamma_\mu B_{\text{dif}} t + \phi_b) \cos(\gamma_\mu B_{\text{av}} t + \phi_c) \exp(-\lambda_T t)$$
$$+ A_L \exp(-\lambda_L t),$$

where the amplitude A_T (A_L) is proportional to the fraction perpendicular (parallel) to the initial polarization direction, J_0 is a Bessel function of the first kind, $\gamma_\mu (= 2\pi \times 135.53$ MHz/T) is the muon gyromagnetic ratio, φ_b (φ_c) is the initial phase of each function, respectively, and λ_T (λ_L) is
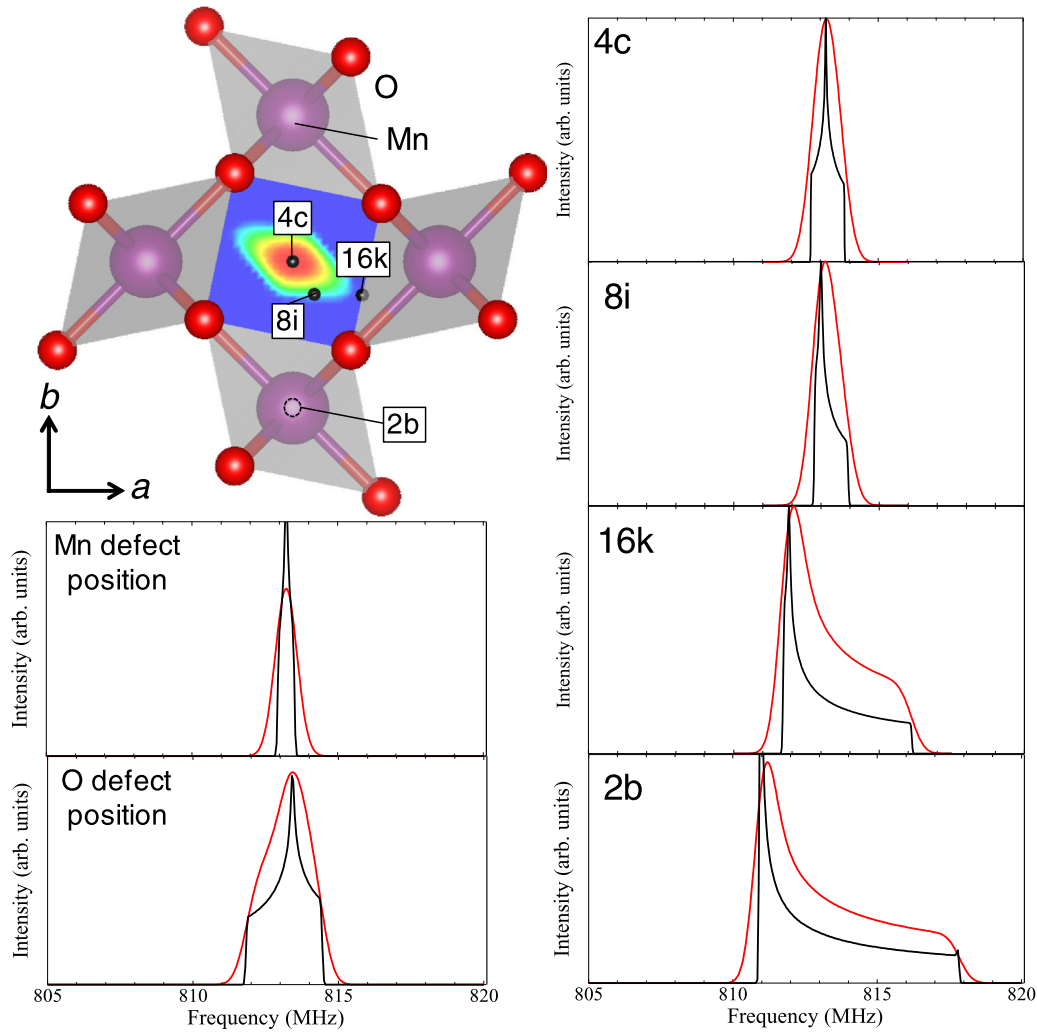
FIG. 3. Simulated powder patterns for the putative muon stopping sites in β-MnO$_2$ under a transverse field of 6 T. Each interstitial crystallographic position is represented in a Wyckoff letter: 4c (1/2,0,0), 8i (0.426 67,0.111 85,0), 16k (0.489 54,0.262 99,0.187 54), 2b (0,0,1/2). The black lines represent the calculated powder patterns. The red lines represent the additional Gaussian broadening (see the main text) superimposed on the powder patterns.
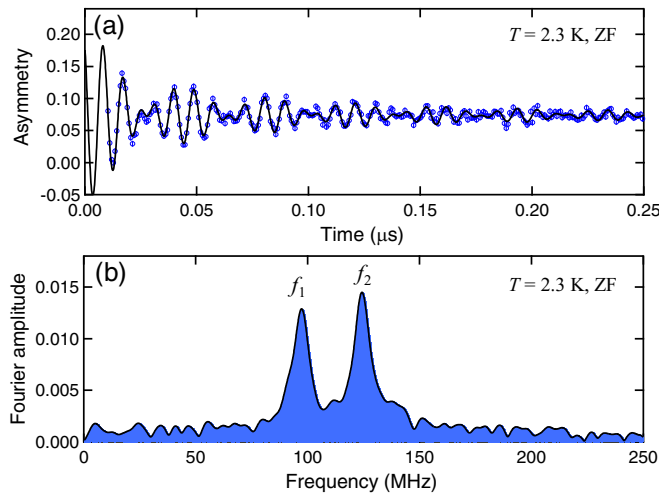

FIG. 4. (a) μSR time spectrum at 2.5 K under a zero external field. The solid line represents the result of least-squares fitting (see the main text). (b) Fast Fourier transform of the time spectrum. f_1 (f_2) indicates a peak frequency.

the transverse (longitudinal) relaxation rate. The solid curve in Fig. 4(a) shows the result of a least-squares curve-fit. The temperature dependence of the respective parameters below T_N are shown in Fig. 5.

The slight decrease of A_T at lower temperatures is attributed to the partial loss of initial muon polarization (which is discussed below). The development of the magnetic order parameter with decreasing temperature manifests in the evolution of the frequency $\gamma_\mu B_{av}$ as shown in Fig. 5(c). The temperature dependence of $\gamma_\mu B_{av}$ shows a critical behavior described by the power law, $\gamma_\mu B_{av}(T) \propto (T_N - T)^\beta$ with $T_N = 92.7(2)$ K and $\beta = 0.182(9)$. The value of critical exponent β is in good agreement with those obtained from the synchrotron x-ray magnetic scattering [26] and the neutron scattering [27]. Although the phase parameter φ_c is nearly zero except around T_N, φ_b tends to be shifted by $\sim\pi/4$ compared with φ_c. It may be related to the $\pi/4$ phase shift between the Bessel function and the cosine function [36].

The temperature dependences of the observed signal fraction, $[A_T + A_L]/A_0$ (red circle), and the longitudinal fraction,
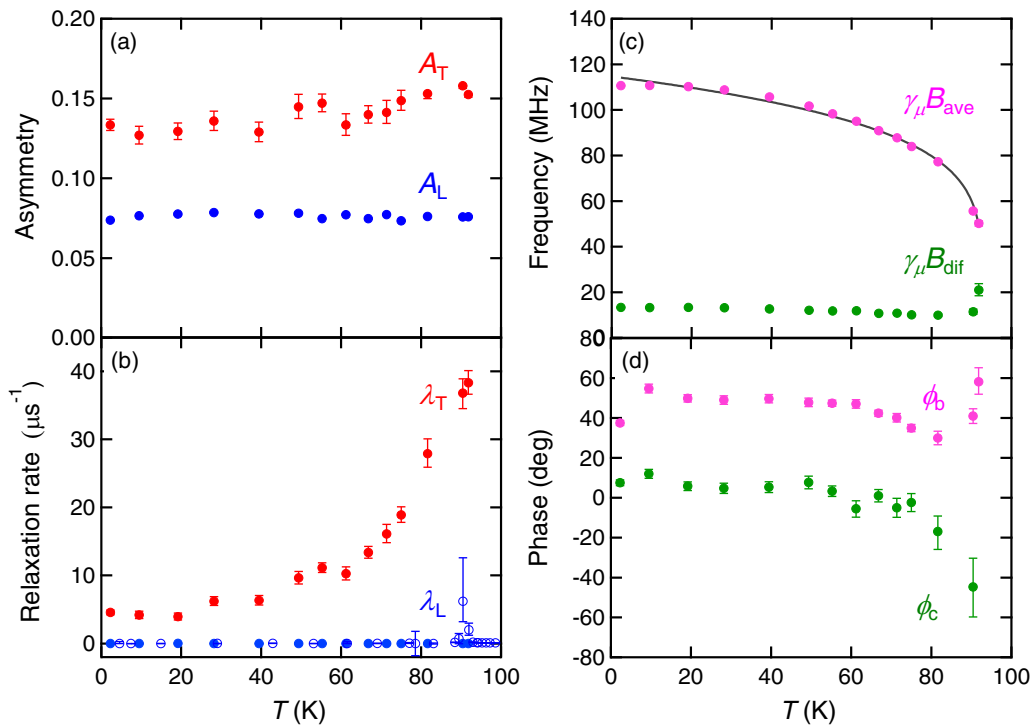
FIG. 5. Temperature dependence of (a) the transverse (longitudinal) asymmetry A_T (A_L), (b) the transverse (longitudinal) relaxation rate λ_T (λ_L), (c) the precession frequencies $\gamma_\mu B_{av}$ and $\gamma_\mu B_{dif}$, and (d) the initial phase φ_b and φ_c. The open circle in (b) indicates λ_L obtained at J-PARC MUSE. The solid line in (c) indicates the result of a least-squares curve-fit by the power-law function (see the main text).

A_L/A_0 (blue circle), are shown in Fig. 6, where A_0 (=0.23) is estimated from the full asymmetry above T_N. One can clearly see that the signal fraction below T_N is less than 90% of the

FIG. 6. Temperature dependence of the observed signal fraction (red circle) and the longitudinal signal fraction f_L (blue circle). The inset shows the enlargement below 50 K with the fitting curve using the thermal activation model (see the main text). The broken line represents 1/3 of the total fraction.

total volume fraction. In contrast, the longitudinal fraction (z component) is almost one-third of the total volume fraction, indicating that all the implanted muons are subject to isotropic static magnetic order. These facts indicate that there is an unresolved signal component (missing fraction) that is depolarized within the dead time ($t < 0.01$ μs) of the experiment.

The missing fraction at 2.3 K is estimated to be about 15% of the total volume fraction. Such a fast depolarization is attributed to the strong disorder of $D(B_{loc})$. Considering that the possibility of muons occupying an O vacancy is unlikely, as inferred from $D(B_{loc})$ (at least above T_N; see Fig. 3), it is reasonable to attribute the origin of the missing fraction to the muons occupying Mn vacancies, which corresponds to naturally included Ruetschi protons. This also leads to the hypothesis that the residual 85% of muons corresponds to interstitial hydrogens (Coleman protons), which occupy the oxygen channels.

Upon close examination of the temperature dependence of A_L/A_0 in Fig. 6, one can see that it slightly declines from the one-third line as temperature decreases. This is attributed to the formation of a paramagnetic Mu^0 state, which is subject to the spin/charge exchange process with a diamagnetic state ($Mu^+ + e^- \rightarrow Mu^0$). The reduction of A_L strongly suggests that the electronic state bound to the interstitial muon is not polaronic (i.e., the electron spin not being locked along the Mn spins), but rather atomic to allow the spin-triplet ($F = 1$) or spin-singlet ($F = 0$) state relative to the muon spin direction. The precession frequency for the $F = 0$ state usually exceeds the limit determined by experimental time resolution [38]. Therefore, only residual polarization for the $F = 1$ state can be observed, resulting in a reduction of the longitudinal
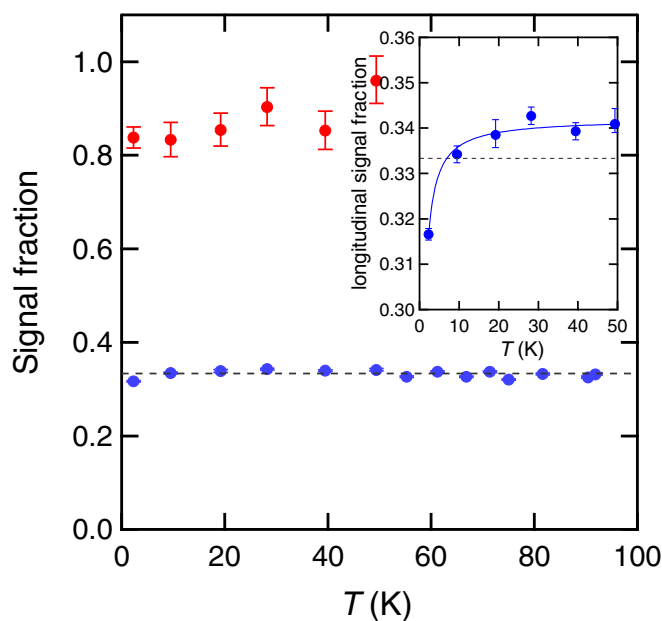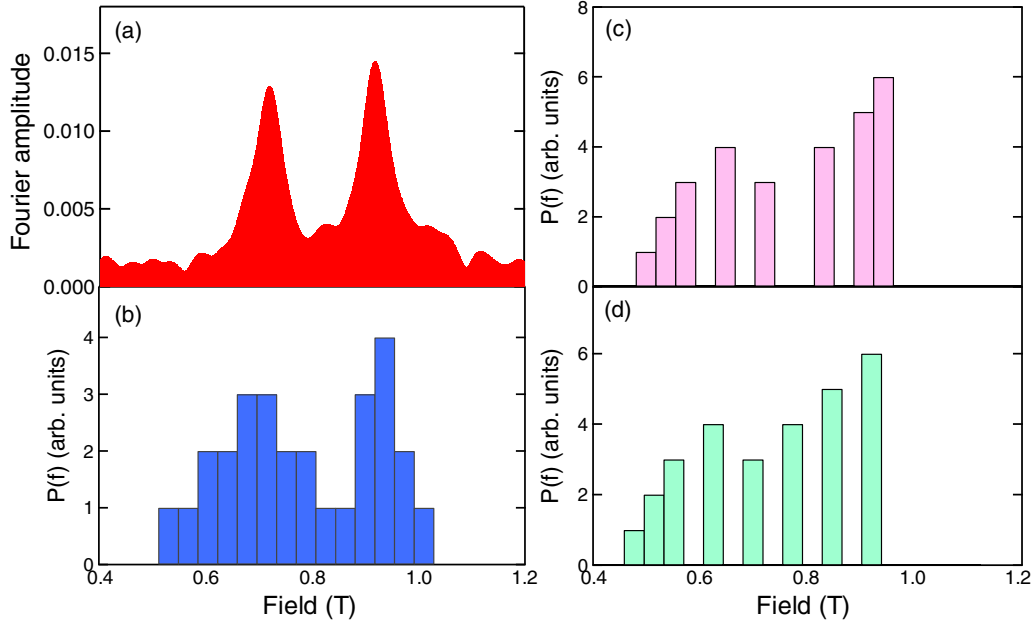
FIG. 7. (a) Local field distribution (B_{loc}) at 2.3 K under a zero external field. (b) Simulated distribution of B_{loc} at the $4c$ site. Simulated distribution of B_{loc} at the structurally optimized site with a polaronic electron (not obtained from the DFT calculation) distributed on the nearest Mn ion only (c) or the nearby three Mn ions (d).

fraction by half. If Mu^0 is present, the longitudinal asymmetry A_L is reproduced by the following linear combination:

$$A_L = \tfrac{1}{3}\left(1 - \tfrac{1}{2}f_{Mu}\right)A_0,$$

where f_{Mu} is the fractional yield of Mu^0.

The temperature dependence of the longitudinal signal fraction f_L (see Fig. 6, inset) is adequately described by the thermal activation model $f_L = f_d \exp(-E_a/2k_B T)$, where f_d is the diamagnetic longitudinal fraction ($f_L = f_d$, when $f_{Mu} = 0$), E_a is the characteristic energy, and k_B is Boltzmann's constant. A fit of f_L (blue line in the inset of Fig. 6) below 50 K yields $f_d = 0.3420(8)$ and $E_a = 0.0292(8)$ meV/K. Considering the value of $f_L = 0.316(1)$ at 2.3 K, f_{Mu} is estimated to be 0.0760(4) (which may be a lower bound for the Mu^0 yield). This means that the electrons from the hydrogen impurity levels are mostly promoted to the conduction band in most temperature ranges. In other words, the donor level associated with hydrogen is estimated to be extremely shallow, probably less than 0.1 meV. Since the diamagnetic muons in the oxygen channels (corresponding to the Coleman proton) can be attributed to Mu^0 in its ionized state, they are presumed to serve as electron donors. For these reasons, interstitial hydrogen is expected to be a source of *n*-type conductivity in β-MnO_2. We note that the hydrogen concentration (2.918×10^{19} cm^{-3}) obtained from our TDS measurement is comparable with the carrier density ($n = 4.8 \times 10^{19}$ cm^{-3}) reported in Ref. [24], which is perfectly in line with this scenario.

C. First-principles calculations

To gain a better understanding of hydrogen states in β-MnO_2, DFT calculations were performed using VASP for comparisons with the μSR experiments. As the first step, we calculated the local field B_{loc} at the most energetically stable

position $4c$ $(1/2,0,0)$ with the screw periodicity $q = 2c^*/7$ and an Mn^{4+} moment size of $2.34\mu_B$ [27]. Under zero external field, B_{loc} is determined by a vector sum of the magnetic dipolar field of the Mn ions and the Fermi contact interaction with an unpaired electron in the muon $1s$ orbital [39],

$$B_{loc} = \sum_i \hat{A}_i \mu_i + \frac{8}{3}\pi S_e \delta(r),$$

where μ_i is the magnetic moment of the ith Mn ion located at distance $r_i = (x_i, y_i, z_i)$ from the muon site, S_e is the electron spin magnetic moment, $\delta(r)$ is the delta function, and

$$\hat{A}_i = A_i^{\alpha\beta} = \frac{1}{r_i^3}\left(\frac{3\alpha_i\beta_i}{r_i^2} - \delta_{\alpha\beta}\right) \ (\alpha, \beta = x, y, z)$$

is the dipolar tensor. The Fermi contact term is basically negligible except for the Mu^0 state.

Figure 7(b) shows a simulated distribution of B_{loc} for the $4c$ site, which is in remarkable agreement with the experimental result [Fig. 7(a)]. A comparative study with DFT calculation provides useful information for identifying the muon's location and state. For example, if all the nn Mn^{4+} ($S = 3/2$) ions bear the full moment ($3\mu_B$), the calculated distribution of B_{loc} becomes broader, leading to a shift of the central frequency by $\sim$30 MHz (not shown), which is in disagreement with the experimental result. This also supports the moment reduction of Mn ions ($2.34\mu_B$) from the viewpoint of local magnetism probed by μSR.

We further extended the simulation of B_{loc} to investigate the influence of structural relaxation by a muon/hydrogen insertion. The Brillouin zone for a $2 \times 2 \times 3$ supercell was sampled using a cutoff energy of 500 eV and a $4 \times 4 \times 4$ k-point mesh for calculations. The structure optimization was performed using lattice parameters, and all of the atomic po-
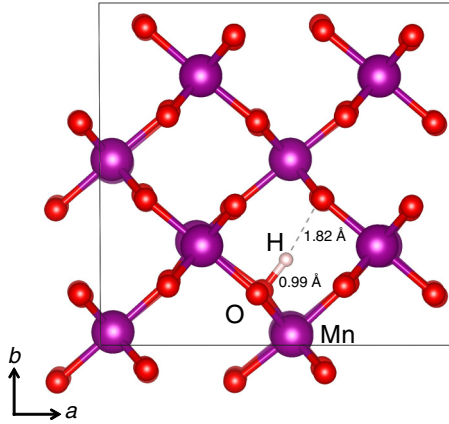
FIG. 8. Deformation of the host lattice on hydrogen intercalation inferred from the DFT (VASP) calculation. The broken line represents the H–O hydrogen bond.

sitions were allowed to relax until the forces acting on each ion became less than 0.01 eV/Å. Note that the spin degree of freedom and the electron correlation parameter U are not incorporated, because the difference between the optimized atomic positions of Mn around the hydrogen is small irrespective of the presence or absence of U (=4 eV). Therefore, it is not an issue in this study.

The result of the calculation is shown in Fig. 8. The hydrogen occupies slightly off-center of the oxygen channel, where it forms an O–H bond with a bond length of 0.99 Å, and it donates an electron to the host lattice. The surrounding oxygens show large displacement from their initial crystallographic positions due to the hydrogen bond. On the other hand, the surrounding cationic sublattice of Mn ions shows a slight expansion due to the electrostatic repulsion between the H^+ and Mn^{4+} ions, resulting in 1.4–7.2 % Mn-Mn bond elongation compared to those without H insertion. Taking into account the displacement of six neighboring Mn ions from H, we have simulated B_{loc} using a 686-octahedron $7 \times 7 \times 7$ supercell to reproduce the partially distorted β-MnO$_2$ lattice considering the period of the helical magnetic structure.

When a muon (or hydrogen) is bound to an oxygen, the donated electron can localize on a neighboring transition-metal d orbital to form a charge-neutral complex (i.e., a polaron) [17,18,40]. In light of this possibility, we simulated B_{loc} with two different charge distributions: a polaronic electron distributed on the nn Mn ion only [Fig. 7(c)], or the nearby three Mn ions [Fig. 7(d)], which are not obtained from the DFT calculation. Although subtle differences in shape are observed in comparison with the nondistorted case [Fig. 7(b)], they still have a characteristic two-peak structure. Note that when the structure was optimized by fixing hydrogen at the $4c$ site, the Mn-H distance was uniformly extended for all the Mn ions. Therefore, no significant change in the shape of the local magnetic field was obtained.

Hydrogen generally takes an asymmetric O-H–O configuration with a short O-H covalent bond and a long H–O hydrogen bond. However, it resides equidistantly between two nearest oxygen atoms under high pressures. This phenomenon is called *H-bond symmetrization*, and it is often observed in the high-pressure phase of ice [41]. The H-bond symmetrization is closely linked to zero-point vibration, thus the isotope effect is expected to be more pronounced [42,43]. For example, δ-AlOOH, which has a distorted-rutile-type framework, shows H-bond symmetrization under high pressures with a significant isotope effect; the deuteration induces a shift of the symmetrization to a higher pressure [44]. It is commonly known that a lighter isotope possesses a larger zero-point energy. The presumption that a muon is located in the middle of two nearest oxygen atoms to form a symmetric O-μ-O bond due to the isotope effect would be a possible scenario to explain the muon localization at the $4c$ site. We have evaluated the zero-point motion energy of a muon and hydrogen from the potential energy distribution along the O-$4c$-O direction by the DFT calculation using VASP (see the Supplemental Material [28], Fig. S4). Given the energy difference between the ground state (E_0) and the first excited state (E_1) of a muon or hydrogen, a muon can tunnel between the two wells at a very fast timescale as long as the muon spin precession frequency is much lower than the tunneling frequency. This picture can be approximated as a kind of resonant state in which a muon is located at the center of the tunnel. In such a case in which the quantum nature is pronounced, the muon may not be able to simulate the behavior of dilute hydrogen defects correctly.

D. Electronic and magnetic states

Finally, we discuss the electronic and magnetic states of β-MnO$_2$ based on the results obtained so far. The formal magnetic moment of Mn^{4+} ions should be $3\mu_B$ as the localized spin system, because β-MnO$_2$ shows an insulating behavior in the low-temperature region ($T < 50$ K). However, the Mn ordered moment is markedly reduced to $2.34\mu_B$ [27], and this fact has been supported by the present μSR result as described above.

The discrepancy in the size of the Mn moment may be attributed to the localized e_g electrons originating from unintended impurity defects. If the Hund coupling is fairly large, e_g electrons can become localized at a part of the Mn sites and perfectly polarized along the localized t_{2g} moments at the expense of their itinerancy [24]. However, massive amounts of impurities or oxygen defects would be required to induce such significant Mn moment reduction ($3\mu_B \rightarrow 2.34\mu_B$). Moreover, Hund coupling usually enhances the magnetic moment, e.g., double-exchange interaction, thus it would lead to a contradictory result. Although there is a possibility that the delocalization effect of t_{2g} electrons remains at low temperatures [24], we can rule this out because our μSR results clearly indicate that the local field distribution of β-MnO$_2$ is well reproduced by the summation of the dipolar interaction from localized Mn moments.

Here, we propose an alternative scenario to explain the Mn moment reduction in β-MnO$_2$. Charge redistribution from a formal valence between a metal and its ligand is a fundamental process in transition-metal oxides [45]. For example, there are slightly trivalent Cu ions (Cu$^{2+}\underline{L}$, $\underline{L}$: a hole on the oxygen ligand sites) in hole-doped high-T_C superconductors [46] or oxygen holes in a Co^{3+}/Co^{4+} mixed valence state in

Li_xCoO_2 [47]. The degree of the charge transfer from a O $2p$ orbital to a transition-metal $3d$ orbital depends on the energy difference between both orbitals, and it also relates to their electronegativity. In the case of Mn^{3+}/Mn^{4+} mixed-valent oxides, significant charge transfer between Mn and O ions has been observed in the x-ray Compton scattering [48]. It is also in good agreement with the theoretical prediction that the Mn–O bond is not purely ionic but partially covalent [49]. Such an intermediate character between an ionic and a covalent Mn-O bond may play an important role in the catalytic activity and the performance for electrochemical storage of manganese oxides.

Based on these facts, we assumed the charge-transfer process occurred from the O $2p$ orbital to the Mn $3d$-t_{2g} orbital in β-MnO_2. If the covalent character of the Mn-O bond suppresses the increase of the Mn^{3+} ionic radius and stabilizes a low-spin electronic configuration (t_{2g}^4) absolutely, the Mn^{3+} moment would be significantly reduced ($2\,\mu_B$) compared to that ($4\,\mu_B$) of a high-spin configuration ($t_{2g}^3e_g^1$). As a reference, a low-spin state of the Mn^{3+} ion is often found in some tunnel-structure manganese oxides [50,51]. The experimental value of the reduced Mn moment ($2.34\mu_B$) in β-MnO_2 can be reproduced by the charge transfer of about 0.1 electron from each of the surrounding six oxygen ions (or even less than this, if the oxygen spin polarization is antiparallel to the Mn spins [52,53]). Further studies of each wave-function character, e.g., Compton scattering, will be required to support our argument.

IV. SUMMARY

We have studied the electronic and magnetic state of β-MnO_2 in terms of hydrogen impurities using the μSR technique combined with first-principles calculations. We have found the following experimental results: (i) 85% of muons localize in the oxygen channels of the rutile structure as interstitial protons, (ii) a residual 15% of muons are associated with lattice imperfection as Mn vacancies, and (iii) 7.6% of those muons (in the oxygen channels) form a charge-neutral Mu state at 2.3 K, which suggests that hydrogen interstitials act as shallow donors whose ionization energy is less than 1 meV. Detailed analyses combined with first-principles calculations showed that implanted muons may prefer the center of the oxygen channel to form a symmetric O-μ-O bond due to a large isotope effect.

[1] E. Hayashi, Y. Yamaguchi, K. Kamata, N. Tsunoda, Y. Kumagai, F. Oba, and M. Hara, J. Am. Chem. Soc. **141**, 890 (2019).

[2] D. Glover, B. Schumm, and A. Kozawa, *Handbook of Manganese Dioxides-Battery Grade* (The International Battery Material Association, Cleveland, 1989).

[3] P. Ruetschi, J. Electrochem. Soc. **131**, 2737 (1984).

[4] P. Ruetschi and R. Giovanoli, J. Electrochem. Soc. **135**, 2663 (1988).

[5] J. J. Coleman, Trans. Electrochem. Soc. **90**, 545 (1946).

[6] F. Fillaux, C. H. Cachet, H. Ouboumour, J. Tomkinson, C. Lévy-Clément, and L. T. Yu, J. Electro-chem. Soc. **140**, 585 (1993).

[7] M. Nagao, C. Pitteloud, T. Kamiyama, T. Otomo, K. Itoh, T. Fukunaga, and R. Kanno, J. Electro-chem. Soc. **152**, E230 (2005).

[8] C. Pitteloud, M. Nagao, K. Itoh, and R. Kanno, J. Solid State Chem. **181**, 467 (2008).

[9] WI. Jung, M. Nagao, C. Pitteloud, K. Itoh, A. Yamada, and R. Kanno, J. Mater. Chem. **19**, 800 (2009).

[10] Y. Paik, J. P. Osegovic, F. Wang, W. Bowden, and C. P. Grey, J. Am. Chem. Soc. **123**, 9367 (2001).

[11] C. G. Van de Walle, Phys. Status Solidi B **235**, 89 (2003).

[12] C. G. Van de Walle, Phys. Rev. Lett. **85**, 1012 (2000).

[13] J. M. Gil, H. V. Alberto, R. C. Vilão, J. P. Duarte, P. J. Mendes, L. P. Ferreira, N. Ayres de Campos, A. Weidinger, J. Krauser, Ch. Niedermayer, and S. F. J. Cox, Phys. Rev. Lett. **83**, 5294 (1999).

[14] S. F. J. Cox, E. A. Davis, S. P. Cottrell, P. J. C. King, J. S. Lord, J. M. Gil, H. V. Alberto, R. C. Vilão, J. Piroto Duarte, N. Ayresde Campos, A. Weidinger, R. L. Lichti, and S. J. C. Irvine, Phys. Rev. Lett. **86**, 2601 (2001).

[15] K. Shimomura, K. Nishiyama, and R. Kadono, Phys. Rev. Lett. **89**, 255505 (2002).

[16] Z. Salman, T. Prokscha, A. Amato, E. Morenzoni, R. Scheuermann, K. Sedlak, and A. Suter, Phys. Rev. Lett. **113**, 156801 (2014).

[17] K. Shimomura, R. Kadono, A. Koda, K. Nishiyama, and M. Mihara, Phys. Rev. B **92**, 075203 (2015).

[18] R. C. Vilão, R. B. L. Vieira, H. V. Alberto, J. M. Gil, A. Weidinger, R. L. Lichti, B. B. Baker, P. W. Mengyan, and J. S. Lord, Phys. Rev. B **92**, 081202(R) (2015).

[19] M. Hiraishi, K. M. Kojima, M. Miyazaki, I. Yamauchi, H. Okabe, A. Koda, R. Kadono, S. Matsuishi, and H. Hosono, Phys. Rev. B. **93**, 121201(R) (2016).

[20] H. Okabe, M. Hiraishi, S. Takeshita, A. Koda, K. M. Kojima, and R. Kadono, Phys. Rev. B **98**, 075210 (2018).

[21] K. M. Kojima, M. Hiraishi, H. Okabe, A. Koda, R. Kadono, K. Ide, S. Matsuishi, H. Kumomi, T. Kamiya, and H. Hosono, Appl. Phys. Lett. **115**, 122104 (2019).

[22] A. F. Wells, *Structural Inorganic Chemistry* (Oxford University Press, Oxford, 1975).

[23] Y. Noda, S. Ohno, and S. Nakamura, Phys. Chem. Chem. Phys. **18**, 13294 (2016).

[24] H. Sato, T. Enoki, M. Isobe, and Y. Ueda, Phys. Rev. B **61**, 3563 (2000).

[25] W. H. Baur, Acta Crystallogr. B **32**, 2200 (1976).

[26] H. Sato, K. Wakiya, T. Enoki, T. Kiyama, Y. Wakabayashi, H. Nakao, and Y. Murakami, J. Phys. Soc. Jpn. **70**, 37 (2001).

[27] M. Regulski, R. Przenioslo, I. Sosnowska, and J.-U. Hoffmann, J. Phys. Soc. Jpn. **73**, 3444 (2004).

[28] See Supplemental Material at http://link.aps.org/supplemental/10.1103/PhysRevB.103.155121 for additional figures.

[29] A. Suter and B. M. Wojek, Phys. Proc. **30**, 69 (2012).

[30] G. Kresse and D. Joubert, Phys. Rev. B **59**, 1758 (1999).

[31] G. Kresse and J. Furthmuller, Phys. Rev. B **54**, 11169 (1996).

[32] J. P. Perdew, K. Burke, and M. Ernzerhof, Phys. Rev. Lett. **77**, 3865 (1996).

[33] K. M. Kojima, J. Yamanobe, H. Eisaki, S. Uchida, Y. Fudamoto, I. M. Gat, M. I. Larkin, A. Savici, Y. J. Uemura, P. P. Kyriakou, M. T. Rovers, and G. M. Luke, Phys. Rev. B **70**, 094402 (2004).

[34] K. Momma and F. Izumi, J. Appl. Crystallogr. **44**, 1272 (2011).

[35] C. P. Slichter, *Principles of Magnetic Resonance*, 3rd ed. (Springer-Verlag, New York, 1990).

[36] A. Yaouanc and P. Dalmas de Réotier, *Muon Spin Rotation, Relaxation and Resonance: Applications to Condensed Matter* (Oxford University Press, Oxford, 2011).

[37] A. Amato, P. Dalmas de Réotier, D. Andreica, A. Yaouanc, A. Suter, G. Lapertot, I. M. Pop, E. Morenzoni, P. Bonfà, F. Bernardini, and R. De Renzi, Phys. Rev. B **89**, 184425 (2014).

[38] A. Schenck, *Muon Spin Rotation Spectroscopy, Principles and Applications in Solid State Physics* (Adam Hilger, Bristol, 1985), p. 215.

[39] R. S. Hayano, Y. J. Uemura, J. Imazato, N. Nishida, K. Nagamine, T. Yamazaki, Y. Ishikawa, and H. Yasuoka, J. Phys. Soc. Jpn. **49**, 1773 (1980).

[40] M. H. Dehn, J. K. Shenton, S. Holenstein, Q. N. Meier, D. J. Arseneau, D. L. Cortie, B. Hitti, A. C. Y. Fang, W. A. MacFarlane, R. M. L. McFadden, G. D. Morris, Z. Salman, H. Luetkens, N. A. Spaldin, M. Fechner, and R. F. Kiefl, Phys. Rev. X **10**, 011036 (2020).

[41] P. Pruzan, J. C. Chervin, and B. Canny, J. Chem. Phys. **99**, 9842 (1993).

[42] M. Benoit, D. Marx, and M. Parrinello, Nature (London) **392**, 258 (1998).

[43] M. Hiraishi, K. M. Kojima, H. Okabe, S. Takeshita, A. Koda, R. Kadono, R. Khasanov, S. Iimura, S. Matsuishi, and H. Hosono, Phys. Rev. B **101**, 174414 (2020).

[44] A. Sano-Furukawa, T. Hattori, K. Komatsu, H. Kagi, T. Nagai, J. J. Molaison, A. M. dos Santos, and C. A. Tulk, Sci. Rep. **8**, 15520 (2018).

[45] A. E. Bocquet, T. Mizokawa, T. Saitoh, H. Namatame, and A. Fujimori, Phys. Rev. B **46**, 3771 (1992).

[46] A. Fujimori, E. Takayama-Muromachi, Y. Uchida, and B. Okai, Phys. Rev. B **35**, 8814(R) (1987).

[47] T. Mizokawa, Y. Wakisaka, T. Sudayama, C. Iwai, K. Miyoshi, J. Takeuchi, H. Wadati, D. G. Hawthorn, T. Z. Regier, and G. A. Sawatzky, Phys. Rev. Lett. **111**, 056404 (2013).

[48] K. Suzuki, B. Barbiellini, Y. Orikasa, N. Go, H. Sakurai, S. Kaprzyk, M. Itou, K. Yamamoto, Y. Uchimoto, Y. J. Wang, H. Hafiz, A. Bansil, and Y. Sakurai, Phys. Rev. Lett. **114**, 087401 (2015).

[49] Y. Liu, T. Fujiwara, H. Yukawa, and M. Morinaga, Solid State Ion. **126**, 209 (1999).

[50] R. D. Shannon and C. T. Prewitt, Acta Crystallogr. B **25**, 925 (1969).

[51] A. D. Wadsley, Acta Crystallogr. **6**, 433 (1953).

[52] M. Miyazaki, R. Kadono, M. Hiraishi, A. Koda, K. M. Kojima, K. Ohashi, T. Takayama, and H. Takagi, Phys. Rev. B **91**, 155113 (2015).

[53] Y. Ishii, S. Horio, Y. Noda, M. Hiraishi, H. Okabe, M. Miyazaki, S. Takeshita, A. Koda, K. M. Kojima, R. Kadono, H. Sagayama, H. Nakao, Y. Murakami, and H. Kimura, Phys. Rev. B **101**, 224436 (2020).